CrystEngComm

Accepted Manuscript

ROYAL SOCIETY OF CHEMISTRY

www.rsc.org/crystengcomm

Hydrothermal Synthesis of Porous *rh*-In_2O_3 Nanostructures with Visible-light-driven Photocatalytic Degradation of Tetracycline

Miaomiao Wu, Chao Wang, Yong Zhao, Lisong Xiao, Chao Zhang, Xiaoqiang Yu, Bifu Luo, Bo Hu, Weiqiang Fan, Weidong Shi*

School of Chemistry and Chemical Engineering, Jiangsu University, Zhenjiang 212013, People's Republic of China

Corresponding author Tel.: +86 511 88791800, Fax: +86 511 88791800

E-mail: swd1978@ujs.edu.cn

Abstract

In this paper, well-defined 3D flower-like porous rhombohedral In_2O_3 (*rh*-In_2O_3) nanostructures were successfully synthesized via the hydrothermal method combining with post-thermal treatments. Interestingly, 3D flower-like *c*-In_2O_3 nanostructures could be also obtained by simply adjusting the annealing temperature according to this reaction route. The possible growth mechanism of obtained flower-like In_2O_3 nanostructures was proposed based on a series of contrasting experimental observations depending on the different reaction conditions as well as our understandings. What's more, we also investigated the photocatalytic activities of bulk In_2O_3, 3D flower-like *rh*-In_2O_3, and *c*-In_2O_3 nanostructures for the degradation of tetracycline (TC) under the visible light. Photocatalytic degradation results indicated that 3D flower-like porous *rh*-In_2O_3 nanostructures exhibited the highest photocatalytic activities. The possible photocatalytic mechanism for the degradation of TC of 3D flower-like porous *rh*-In_2O_3 nanostructures was also discussed.

Keywords: Hydrothermal synthesis, 3D nanostructures, *rh*-In_2O_3, visible light, photocatalysis.

Introduction

Over the past decades, antibiotics have been commonly used to prevent animal diseases and promote livestock productivity [1-3]. However, the frequent occurrence of antibiotics in the aqueous environment leads to the emergence of environmental issues, such as ecological disturbance and water pollution [4-6]. Tetracycline (TC), one of antibiotic groups, is important because of its extremely high consumption as human and veterinary medicines [7-10]. In addition, tetracycline hydrochloride residues may cause a series of ecological, environmental and health issues [11-14].It has drawn widely attention to find a green, low-cost and effective method to remove the tetracycline residues from the aqueous environment. It is well known that photodegradation of tetracycline by semiconductor photocatalysts is an economic and ecologically safe option for solving energy and pollution problems [15-17]. Recently, some studies on the high-efficiency photocatalytic degradation of TC by semiconductor-based (such as TiO_2 and ZnO) photocatalysts have been reported [18-20], but most of them are UV-light driven rather than visible-light driven. Therefore, seeking the available photocatalysts with superior visible-light photocatalytic activities is still a huge challenge.

In_2O_3, as an important n-type semiconductor with wide band gap, has been widely applied in optoelectronic devices such as solar cells [21], touch displays [22], gas sensors [23], and photocatalysts[24]. It exists in either cubic bixbyite-type (*c*-In_2O_3) phase (E_g : 2.93 ± 0.15 eV) or *rh*-In_2O_3 phase (E_g : 3.02 ± 0.15 eV) [25]. For *c*-In_2O_3, various morphologies of *c*-In_2O_3 nanostructures have been obtained through using several approaches, including physical evaporation technique [26], chemical vapor deposition [27], thermal oxidation [28], laser ablation technique [29], sol–gel method [30], and solution-phase growth [31]. However, compared with *c*-In_2O_3, a few studies on *rh*-In_2O_3 nanostructures had been reported because the synthesis of *rh*-In_2O_3 needed some extreme reaction conditions, such as high pressure or high temperature [32]. Usually, solvothermal method has been proved powerful to produce highly pure *rh*-In_2O_3 with uniform densities at low processing temperature [33]. For example, Chen and co-workers prepared rod-like *rh*-In_2O_3 nanostructures by using the Poly-ethylene-glycol (PEG) [34]. Yin synthesized hollow *rh*-In_2O_3 nanostructures via ethanol-glycerol-assisted solvothermal route [35]. Unfortunately, solvothermal method is limited to using many organic or toxic solvents such as triethylene glycol, glycerol, and ethylene glycol, which might bring about great difficulties to the large-scale production and environmental protection [36-38]. Hydrothermal method is a very green, facile, and promising soft chemical route in terms of low reaction temperature, environmentally friendly treatment and large-scale production [39]. However, to the best of our knowledge, no studies on the synthesis of *rh*-In_2O_3 nanostructures through the hydrothermal method have been reported to date.

3D nanostructures including hierarchical rod-aggregates, hexagonal-like and urchin-like nanostructures, have

attracted much interest because 3D structures can affect the surface area, adsorption, reflectance, adhesion, and carrier transportation properties that differ from those of the one-dimensional (1D) or two-dimensional (2D) nanostructures and have enormous potentials in photocatalytic field [40-43]. Herein, well-defined 3D flower-like porous *rh*-In_2O_3 nanostructures self-assembled by nanosheets were successfully prepared via a hydrothermal method combining with post-thermal treatment. Especially, 3D flower-like *c*-In_2O_3 nanostructures could be also obtained by simply adjusting the annealing temperature. Moreover, we explored the effect of the reaction time and the amount of urea and glucose in detail, which played an important role in controlling the shape of 3D flower-like porous *rh*-In_2O_3 nanostructures. The possible growth mechanism of 3D flower-like In_2O_3 nanostructures was studied on the basis of our experimental observations. The photocatalytic activities of 3D flower-like In_2O_3 nanostructures towards the degradation of TC under visible light were reported for the first time. In addition, the photocatalytic degradation results indicated that 3D flower-like porous *rh*-In_2O_3 nanostructures exhibited the highest visible-light-driven photocatalytic performance.

Experimental Details

Preparation of 3D flower-like precursor

All reagents were of analytical grade without further purification and the deionized water was used in all experiments. In a typical synthesis, $In(NO_3)_3$•$4.5H_2O$ (1 mmol), urea (7 mmol), and glucose (9 mmol) were dissolved in 30 mL deionized water (DI water) and stirred at room temperature for 30 min. The resultant solution was transferred into a Teflon-lined stainless steel autoclave (50 mL capacity) and heated at 180 °C for 6 h. As soon as the autoclave was cooled to the room temperature naturally, the products were collected by centrifugation and then washed thoroughly with DI water and ethanol alternately for three times. The products were dried at 60 °C in vacuum for 12 h.

Preparation of 3D porous flower-like *rh*-In_2O_3 nanostructures

The pre-synthesized brown sample was loaded in a quartz boat and annealed in a tube furnace at 500 ºC for 2 h. And then it was cooled to room temperature naturally. The heating rate for the tube furnace was 2 ºC/min before the furnace temperature reached 500 ºC. The final products were collected for subsequent characterization.

Preparation of 3D flower-like *c*-In_2O_3 nanostructures

The pre-synthesized brown sample was loaded in a quartz boat and annealed in a tube furnace at 600 ºC for 2 h. And then it was cooled to room temperature naturally. The heating rate for the tube furnace was 2 ºC/min before the furnace temperature reached 600 ºC. The final products were collected for subsequent characterization.

Preparation of bulk In_2O_3

An appropriate amount of $In(NO_3)_3 \cdot 4.5H_2O$ was loaded in a quartz boat and annealed in a tube furnace at 500 ºC for 2 h. And then it was cooled to room temperature naturally. The heating rate for the tube furnace was 2 ºC/min before the furnace temperature reached 500 ºC.

Sample Characterization

The X-ray powder diffraction (XRD) patterns were performed on Bruker or D8 Advance using Cu-*Kα* radiation (λ =1.54056 Å) in the 2θ range of 10 º to 80 º. The morphologies and microstructures of the samples were characterized by scanning electron microscopy (SEM), transmission electron microscopy (TEM), higher-magnification transmission electron microscopy (HRTEM) images and energy-dispersive X-ray spectrum analysis (EDS). The SEM and EDS were performed using S-4800 II field-emission scanning electron micro-analyzer with the accelerating voltage of 15 kV (Hitachi S4800). The TEM images and HRTEM images were taken on JEOL JEM-2100F high-resolution transmission electron microscope. Specimens for TEM and HRTEM measurements were prepared via drop casting a droplet of an ethanol suspension onto a copper grid, coated with a thin layer of amorphous carbon film, and allowed to dry in air. Raman spectra were collected at room temperature on a Jobin-Yvon HR-800 spectrometer with a 488 nm Ar^+ ion laser. The Brunauer-Emmett-Teller (BET) surface areas were measured with Builder 4200 instrument at liquid nitrogen temperature. Shimadzu UV-2550 spectrometer equipped with WASR-2200 diffuse reflection integrating sphere was employed to acquire the diffuse-reflection ultraviolet-visible (UV-vis) absorbance spectrum of the samples over the range of 200–800 nm, using $BaSO_4$ as a reflection reference.

Photocatalytic activities

The photocatalytic activity measurements of 3D flower-like porous *rh*-In_2O_3 nanostructures, 3D flower-like *c*-In_2O_3 nanostructures and bulk In_2O_3 nanostructures were carried out by degrading the tetracycline (TC, AR.) under visible light irradiation. 50 mg photocatalyst was ultrasonically dispersed in 100 mL Pyrex glass vessel which contained 10 mL tetracycline solution (100 mg•L^{-1}). The solution was continuously magnetically stirred in

dark for about 30 min at room temperature to ensure the establishment of an adsorption–desorption equilibrium. The mixture was then loaded in an open beaker and continuously stirred during the exposure to visible light from a 350 W Xe lamp with a 420 nm cutoff filter and the whole photocatalytic reaction was conducted at room temperature. The distance between the light source and the bottom of the solution was about 10 cm. Absorption spectra of samples were measured to monitor the photocatalytic degradation of TC aqueous solution, and the absorption at 357 nm was recorded as a function of irradiation time.

Results and discussion

Phase and purity of the samples

XRD was performed to investigate the crystal structure of the samples. The XRD pattern of precursor before annealing showed the broad peak centered at around 25° , which was attributed to the (002) plane of the carbon structure (denoted as *). The other main diffraction peaks at 2θ= 22.3°, 31.7°, and 51.2° could be perfectly indexed to the (200), (220), and (420) crystal faces of $In(OH)_3$ (JCPDS No. 73-1810), and the characteristic peaks were relatively weak due to the existence of carbon layer (Fig. 1a). After annealing at 500 °C for 2 h, the diffraction peaks in Fig. 1b were in good agreement with rhombohedra phase of In_2O_3 (*rh*-In_2O_3, JCPDS No. 21-0406), and no characteristic peaks for impurity, such as carbon and $In(OH)_3$ were observed, indicating that the $In(OH)_3$ precursor was completely transformed into *rh*-In_2O_3 under this particular annealing condition. After the subsequent annealing at 600 °C for 2 h, diffraction peaks of *rh*-In_2O_3 disappeared (Fig. 1c), and the new corresponding diffraction peaks could be well indexed to cubic In_2O_3 (*c*-In_2O_3, JCPDS No. 06-0416). It demonstrated that the transformation from $In(OH)_3$ to *rh*-In_2O_3 or *c*-In_2O_3 could be realized via controlling the annealing temperature.

To further examine the different crystalline structures of In_2O_3, Raman spectroscopy measurements were performed on the *rh*-In_2O_3 and *c*-In_2O_3 samples (Fig. 2). On the basis of the group theory analysis, the optical modes of *rh*-In_2O_3 have the irreducible representation, shown as below [44]:

$$\Gamma_{opt} = 2A_{1g} + 5E_g + 2A_{1u} + 2A_{2u} + 3A_{2g} + 4E_u \quad (1)$$

Where the A_{1u}, A_{2u}, A_{2g}, and E_u are infrared active or Raman inactive, the A_{1g} and E_g are Raman active. As shown in Fig. 2a, the Raman mode at 163 and 501 cm^{-1} were attributed to the A_{1g} mode, while the Raman modes at 219, 384, and 590 cm^{-1} were assigned to the E_g mode, which agreed well with the reported values in the literature. What's more, the Raman peaks were relatively weak in intensity due to the incident light scattering caused by the

self-assembled nanostructures constituting the hierarchical structure.

For *c*-In_2O_3, the following vibration modes were predicted [44]:

$$\Gamma_{opt}=4A_g + 4E_g +14T_g +5A_u +5E_u +16T_u \quad (2)$$

Where A_g, E_g, and T_g represent Raman-active modes, Au and E_u represent inactive modes, and T_u represents infrared-active modes. Fig.2b showed representative Raman spectra of *c*-In_2O_3 in the frequency range of 100–700 cm^{-1}. It was very obvious that Raman modes located at about 108, 132, 306, 365, 495, and 627cm^{-1} were in good agreement with Raman active modes of previously described *c*-In_2O_3 structures, which also actually provided additional proof to illustrate the In_2O_3 with cubic phase.

The morphology of the as-obtained samples

The size and morphology of precursor $In(OH)_3$, *rh*-In_2O_3, and *c*-In_2O_3 were investigated by SEM measurement, respectively. As shown in Fig.3a, it could be clearly seen that $In(OH)_3$ obtained by hydrothermal process is orderly flower-like aggregate composed of nanosheets with the coarse surface. After annealing at 500 °C for 2 h (Fig. 3b), the product *rh*-In_2O_3 exhibited well-defined flower-like structures and the EDS spectrum further confirmed the presence of In and O elements in this sample (C and Pt signals come from the plated element for SEM measurement) (Fig. 3d). After annealing at 600 °C for 2 h, the whole morphology of *c*-In_2O_3 was similar with that of the *rh*-In_2O_3 (Fig. 3c). Careful observation on the TEM images of *rh*-In_2O_3 (Fig. 4a and 4b) revealed that the as-prepared flower-like *rh*-In_2O_3 nanostructures were built up by interlaced nanosheets with average thickness of about 100 nm and length of several hundred nanometers. More importantly, these nanosheets were composed of numerous small nanoparticles and many nanopores with the diameter of 5-20 nm appeared (Fig. 4c). Besides, the HRTEM image presented well-defined lattice fringes with an interplanar distance of 0.288 nm, corresponding to the (104) plane of *rh*-In_2O_3 (Fig. 4d), which also indicated the good crystallinity of *rh*-In_2O_3. In addition, the well-arranged SAED image (inset of Fig. 4b) reveals the polycrystalline of the as-obtained *rh*-In_2O_3.

Growth mechanism and factors influencing on the formation of 3D flower-like porous *rh*-In_2O_3 nanostructures

In this work, the possible formation mechanism of 3D flower-like *rh*-In_2O_3 nanostructures was divided into two processes. Firstly, the $In(OH)_3$ precursor with nanosheet-based flowers was prepared by a simple hydrothermal

route. Then, flower-like *rh*-In_2O_3 nanostructures were obtained under ambient pressure by the thermal decomposition of the $In(OH)_3$ precursor at 500 °C for 2 h. In order to understand the formation of 3D flower-like *rh*-In_2O_3 nanostructures, we studied the influence of different parameters on the morphology of products systematically. We found that the reaction time, the amount of urea and glucose both played an important role in controlling the morphology of In_2O_3 nanostructures.

The influence of reaction time on the formation of 3D flower-like In_2O_3 nanostructures was investigated as a variable while keeping all other reaction parameters the same. When the reaction time is less than 20 min, no precipitate was observed. When the reaction time reached 30 min, some leaf-like sheets formed gradually (Fig.5a). When the reaction time was increased to 1 h (Fig. 5b), both some nanosheets and flower-like aggregates appeared. Finally, as the reaction time prolonged to 4 h (Fig. 5c), the individual nanosheets disappeared completely and the well-defined 3D flower-like morphology appeared. Fig. 5d shows the XRD patterns of the products obtained at 30 min, 1 h, and 4 h, respectively. It should be noted that the product before calcination existed in the form of $In(OH)_3$ for different hydrothermal durations.

The influence of glucose on the formation of 3D flower-like *rh*-In_2O_3 nanostructures was investigated as a variable while keeping all other reaction parameters the same. Fig. 6 showed SEM images of the obtained samples under adding the different amount of glucose. Without glucose, the obtained product mainly consisted of irregular and coarse aggregates. When the amount of glucose was 3 mmol, numerous nanosheets appeared. When the amount of glucose was increased to 7 mmol, typical flower-like In_2O_3 nanostructures assembled by nanosheets appeared gradually. However, when the amount of glucose was further increased in 12 mmol, nanosheet-based In_2O_3 flowers can be obtained while individual nanosheets or fragments do exist in the product. It is well known that glucose molecules have a certain binding affinity to indium ion and can be absorbed onto the nanoparticles surfaces when they start growing, achieving anisotropic crystal growth kinetically. When the concentration of glucose was low, the nanosheets were difficult to assemble into flower-like as low rate of nucleation. However, the high rate of nucleation would destroy the formation of 3D flower-like due to the high rate of nucleation. Therefore, when the amount of glucose was 9 mmol, the rate of nucleation was suitable for obtaining the well-defined 3D flower-like structures.

To explore the role of urea in the formation of 3D flower-like In_2O_3, several experiments with different amounts of urea such as 0, 1, 4, and 10 mmol with the other conditions unchanged were conducted (Fig. 7).

Without addition of urea, the product consisted of many sphere-like particles with irregular size. When the amount of urea was 1 mmol, both the aggregated-spheres and aggregated-nanosheets appeared. When further increase the amount of urea (4 mmol), the aggregates disappeared and nanosheets-based flowers grown out gradually. However, further increasing the amount of urea to 10 mmol led to the formation of the mixture of nanosheet-based flowers and several individual nanosheets due to the collapse of flowers. The experimental results revealed that urea played an important role in controlling the morphology of In_2O_3 and well-defined 3D flower-like structure could be achieved successfully with 7 mmol urea. Under the hydrothermal condition, urea could decompose into $NH_3 \cdot H_2O$ and CO_2 (reaction 3). Then $NH_3 \cdot H_2O$ released OH^- and successively reacted with In^{3+} to form $In(OH)_3$ (reaction 4).

$$NH_2(CO)NH_2 + 3H_2O \rightarrow 2NH_4^+ + 2OH^- + CO_2 \uparrow \quad (3)$$

$$In^{3+} + 3OH^- \rightarrow In(OH)_3 \quad (4)$$

From the above-mentioned chemical reactions, we can deduce that the concentration of OH^- is crucial for the formation of $In(OH)_3$ precursor. On one hand, when the addition of urea was not sufficient, the concentration of OH^- was not enough for the full growth of nanosheets. So, it was difficult to assemble into flower-like structure due to low rate of nucleation, which finally led to the formation of sphere-like particles (Fig. 7a). On the other hand, the assembly rate of nanosheets was too fast which led to the collapse of some flower-like structures when excessive urea was introduced. Herein, 7 mmol of urea is appropriate for the formation of 3D flower-like nanostructures.

On the basis of the results discussed above, the possible formation mechanism of flower-like In_2O_3 nanostructures is suggested (Scheme 1). At the initial stage of hydrothermal reaction, because glucose molecules have a certain binding affinity to In^{3+} and can be absorbed onto the nanocrystals surfaces when nanocrystals start growing, achieving anisotropic crystal growth kinetically. At the same time, as the Lewis base, urea can coordinate with the In^{3+} because of the coordination effects [45]. As a result, the complex precursor (such as glucose-In^{3+}-urea) was formed at the initial stage. With the increase of reaction time and temperature, the urea molecules began to hydrolyze to give off OH^-, which favored the homogeneous nucleation of $In(OH)_3$ nanocrystals derived from the complex precursor. As the reaction continued, the $In(OH)_3$ nanocrystals aggregated to form flakes or sheets due to the anisotropy and lots of nanosheets with a planar surface interlaced with each other into a multilayer and network structure. Subsequently, the hierarchical flower-like $In(OH)_3$ structure decorated with carbon layers was shaped by

the self-assembly process. Finally, 3D flower-like porous *rh*-In_2O_3 nanostructures and 3D flower-like *c*-In_2O_3 nanostructures were obtained by annealing at 500 °C and 600 °C for 2 h to remove the carbon layers, respectively.

Photocatalytic activities of 3D flower-like porous *rh*-In_2O_3 nanostructures.

The photocatalytic activities of the as-synthesized 3D flower-like porous *rh*-In_2O_3 nanostructures and 3D flower-like *c*-In_2O_3 nanostructures were evaluated by the degradation of TC (10 mg/L) under visible light irradiation at room temperature. The characteristic absorption peak of TC at λ = 357 nm was selected as monitoring the photocatalytic degradation process of TC. Fig. 8a showed the absorption spectra of the TC aqueous solution in the presence of 3D flower-like *rh*-In_2O_3 nanostructures under visible light irradiation. Obviously, with the increase of degradation time, the absorption peaks at about 357 nm for TC diminished gradually.

The degradation efficiency of TC over 3D flower-like porous *rh*-In_2O_3 nanostructures, 3D flower-like *c*-In_2O_3 nanostructures, and bulk In_2O_3 under visible light irradiation was presented in Fig. 8b. The results showed that the direct photolysis of TC was negligible without a photocatalyst after 3 h visible light irradiation, indicating the stability of TC solution. Meanwhile, in the presence of photocatalysts, the TC concentration decreased steadily with increasing irradiation time. It could be seen that only 19.3% and 41.1% of TC was degraded after 3 h irradiation for the bulk In_2O_3 and 3D flower-like *c*-In_2O_3 nanostructures, respectively. However, for the 3D flower-like porous *rh*-In_2O_3 nanostructures, the TC was degraded by 67.5%, which was greatly more effective than the bulk In_2O_3 and 3D flower-like *c*-In_2O_3 nanostructures.

For TC solution with low concentration, the photocatalytic degradation process was a quasi-first-level reaction and its kinetics could be expressed in the following formula:

$$\ln (C_0/C) = kt \qquad (5)$$

Where the *k* was the apparent rate constant, C and C_0 were the concentration at time and the initial concentration, respectively. Photocatalytic properties of the samples could also be assessed through the reaction rate constant *k* value: the bigger the *k* value, the better the photocatalytic performance. Fig. 8c showed the relationship between $\ln(C_0/C)$ and light time (t). Through the first-level linear fitting, the reaction rate constant *k* values of the products were obtained. As shown in Fig. 8d, the *k* values for bulk In_2O_3, 3D flower-like *c*-In_2O_3 nanostructures, and 3D flower-like porous *rh*-In_2O_3 nanostructures were 0.00748, 0.0692 and 0.1732 h^{-1}, respectively, suggesting that the 3D flower-like porous *rh*-In_2O_3 possessed the highest degradation rate.

It is demonstrated that the photocatalytic activity of individual photocatalytic system is mainly governed by structural features, light absorption ability, and the ability to adsorb target pollutants. To find out the reason for their difference in photocatalytic activity over 3D flower-like *c*-In_2O_3 nanostructures and 3D flower-like porous *rh*-In_2O_3 nanostructures, the UV-vis diffuse reflectance spectrometer (DRS) was first used to determine the band gap energy of these two samples. As shown in Fig. 9, the absorption band edges of 3D flower-like *c*-In_2O_3 and 3D flower-like porous *rh*-In_2O_3 were located at about 430 and 445 nm, respectively. The band gaps energy (E_g) of In_2O_3 was calculated by the plot of $(Ahv)^{1/2}$ versus *hv*, as presented in the inset of Fig. 9. Obviously, the band gaps were estimated to be 2.85 eV for *rh*-In_2O_3 and 2.75 eV for *c*-In_2O_3. It is well acknowledged that the process of photocatalysis for catalysts is the excitation of electrons from valence band to conduction band by direct absorption of photons, and separated electrons and holes subsequently move to the catalyst surface and react with TC. This process is initiated by light absorption with energy equal to or larger than the band gap energy of semiconductors. This means that the narrower band gap, the more active the photocatalyst. However, in our case, the photocatalytic of 3D flower-like porous *rh*-In_2O_3 nanostructures were much higher than that of 3D flower-like *c*-In_2O_3 nanostructures, indicating that the higher photocatalytic was not attributed to the narrower band gap. In addition, nitrogen sorption was then used to measure the Brunauer-Emmett-Teller (BET) surface areas of the 3D flower-like *c*-In_2O_3 nanostructures and 3D flower-like porous *rh*-In_2O_3 nanostructures. It was found that the BET surface area of 3D flower-like porous *r*h-In_2O_3 (27.2 m^2/g) was much larger than that of 3D flower-like *c*-In_2O_3 (19.5 m^2/g). The relatively higher BET surface area of 3D flower-like porous *rh*-In_2O_3 further confirmed that the as-obtained *rh*-In_2O_3 possessed the porous structure. Usually, a higher surface area is beneficial to the reduced probability of electron–hole recombination and promoted migration of photogenerated carriers. Hence, we concluded that the much higher photocatalytic activity of 3D flower-like porous *rh*-In_2O_3 compared with 3D flower-like *c*-In_2O_3 was owing to its larger BET surface area.

Detection of active species by scavengers

In aqueous solution, the photo-assisted catalytic degradation of TC was caused by the active species produced on the surface of semiconductors, such as holes, electrons, •OH, and $•O_2^-$ [46]. When absorbing the visible light with the energy (hv) equal to or larger than the band gap energy (Eg), the 3D flower-like *rh*-In_2O_3 nanostructures generate valence-band holes (h^+) and conduction-band electrons (e^-) at the surface, which is illustrated in the following eqs (7):

$$2In_2O_3 + h\nu \rightarrow In_2O_3\ (h^+_{VB}) + In_2O_3\ (e^-_{CB}) \quad (7)$$

The separation of electrons and holes is always recognized to be the initial step in the photodegradation mechanism. Therefore, to unfold the mechanism of the process, a series of quenchers were employed to ascertain the ruling active species. The scavengers introduced to the TC solution prior to the addition of *rh*-In_2O_3 photocatalyst [47] were benzoquinone (BQ) for $\bullet O_2^-$, EDTA for h^+, $AgNO_3$ for e^-, and tert-butyl alcohol (TBA) for •OH. Fig. 10 is the photodegradation of TC over 3D flower-like porous *rh*-In_2O_3 photocatalyst in the presence of active species scavengers. The addition of BQ and EDTA substantially diminished the photodegradation of TC and a similar inhibition phenomenon was also observed with the addition of TBA. However, the introduction of $AgNO_3$ caused a small increase in the photodegradation of TC.

Directed by the above findings from the active species trapping experimental results, we conclude that the holes, •OH radicals and $\bullet O_2^-$ are the main contributors to the photocatalysis of TC over 3D flower-like porous *rh*-In_2O_3 photocatalyst. It should be noted that the CB electrons of *rh*-In_2O_3 can combine with Ag^+ after introducing the $AgNO_3$, which can effectively separate the electron–hole pairs and refrain the recombination of electrons and holes [48]. In other words, the more holes can be released from the VB of *rh*-In_2O_3 and attend to the photodegradation. On the basis of the above results, we propose a plausible mechanism for the photodegradation of TC over 3D flower-like porous *rh*-In_2O_3 photocatalyst. As shown in the scheme 2, under the irradiation of visible light, the electron–hole pairs are excited from the VB of 3D flower-like porous *rh*-In_2O_3 to its CB. The electron–hole pairs can then undergo further reactions with dissolved oxygen and water to form reactive radical species. The holes can react with water adsorbed on the surface of 3D flower-like porous *rh*-In_2O_3 to generate highly active hydroxyl radicals (•OH). Moreover, O_2 acts as an electron acceptor and generates $\bullet O_2^-$ species, which are found to be the ruling active species in the photodegradation of TC. In addition, the photogenerated holes are also involved in the direct oxidation of TC which is evidenced by the active species trapping experiments. Thus, the active species including holes, •OH radicals, and $\bullet O_2^-$ result in the degradation of TC over 3D flower-like porous *rh*-In_2O_3 photocatalyst under visible light.

Conclusions

In summary, we reported the preparation of well-defined 3D flower-like porous *rh*-In_2O_3 nanostructures self-assembled by numerous nanosheets via a hydrothermal method combining with post-thermal treatment. Interestingly, 3D flower-like *c*-In_2O_3 nanostructures could be also obtained by simply adjusting the annealing

temperature. We explored the effect of the reaction time and the amount of urea and glucose in detail, which significantly influenced the formation of 3D flower-like Porous *rh*-In_2O_3 nanostructures. What's more, the photocatalytic activities of 3D flower-like In_2O_3 nanostructures towards the degradation of TC under visible light irradiation were reported for the first time. 3D flower-like Porous *rh*-In_2O_3 nanostructures exhibited the highest photocatalytic activity for the degradation of TC under the visible light irradiation. It is expected that this repeatable and mild synthesis route could aid to fabricate more efficient photocatalyst with well-defined structures and high photocatalytic performance for environmental remediation.

Acknowledgements

We gratefully acknowledge the financial support of the National Natural Science Foundation of China (21276116, 21477050, 21301076 and 21303074), Excellent Youth Foundation of Jiangsu Scientific Committee (BK20140011), Program for high-level innovative and entrepreneurial talents in Jiangsu Province, Program for New Century Excellent Talents in University (NCET-13-0835), Henry Fok Education Foundation (141068) and Six Talents Peak Project in Jiangsu Province (XCL-025).

Reference

1. A. P. Carter, W. M. Clemons, D. E. Brodersen, R. J. Morgan-Warren, B. T. Wimberly and V. Ramakrishnan, *Nature*, 2000, **407**, 340.
2. I. Chopra and M. Roberts, *Microbiol*. *Mol. Biol. R*., 2001, **65**, 232.
3. H. Goossens, M. Ferech, R. V. Stichele, M. Elseviers and E. P. Grp, *Lancet*, 2005, **365**, 579.
4. J. Harder, J. Bartels, E. Christophers and J. M. Schroder, *J. Biol. Chem*., 2001, **276**, 5707.
5. M. A. Kohanski, D. J. Dwyer, B. Hayete, C. A. Lawrence and J. J. Collins, *Cell*, 2007, **130**, 797.
6. K. K. Kumarasamy, M. A. Toleman and T. R. Walsh, *Lancet. Infect. Dis*, 2010, **10**, 597.
7. K. M. Neuzil, B. G. Mellen, P. F. Wright, E. F. Mitchel and M. R. Griffin, *New. Engl. J. Med*., 2000, **342**, 225.
8. J. D. Rothstein, S. Patel, M. R. Regan, C. Haenggeli, Y. H. Huang, D. E. Bergles, L. Jin, M. D. Hoberg, S. Vidensky, D. S. Chung, S. V. Toan, L. I. Bruijn, Z. Z. Su, P. Gupta and P. B. Fisher, *Nature*, 2005, **433**, 73.
9. A. K. Sarmah, M. T. Meyer and A. B. A. Boxall, *Chemosphere*, 2006, **65**, 725.
10. P. S. Stewart and J. W. Costerton, *Lancet*, 2001, **358**, 135.
11. K. Kuemmerer, *Chemosphere*, 2009, **75**, 417.
12. T. Tikka, B. L. Fiebich, G. Goldsteins, R. Keinanen and J. M. Koistinaho, *J. Neurosci*., 2001, **21**, 2580

13. A. N. Sapadin and R. Fleischmajer, *J. Am. Acad. Dermatol*., 2006, **54**, 258.
14. K. N. Agwuh and A. MacGowan, *J. Antimicrob. Chemoth*., 2006, **58**, 256.
15. Z. Lu, P. Huo, Y. Luo, X. Liu, D. Wu, X. Gao, C. Li and Y. Yan, *J. Mol. Catal. A-Chem*., 2013, **378**, 91.
16. J. Lopez-Penalver, M. Sanchez-Polo, C. V. Gomez-Pacheco and J. Rivera-Utrilla, *J. Chem. Technol. Biot*., 2010, **85**, 1325.
17. Y. Chen, C. Hu, J. Qu and M. Yang, *J. Mater. Chem. A*, 2008, **197**, 81.
18. J. Choina, A. Bagabas, Ch. Fischer, G.-U. Flechsig, H. Kosslick, A. Alshammari and A. Schulz, Catal. Today, 2015, 241, 47.
19. R. A. Palominos, M. A. Mondaca, A. Giraldo, G. Peñuela, M. Pérez-Moya and H. D. Mansilla, Catal. Today, 2009, 144, 100.
20. X. D. Zhu, Y. J. Wang, R. J. Sun and D. M. Zhou, Chemosphere, 2013, 92, 925.
21. C. Li, D. H. Zhang, X. L. Liu, S. Han, T. Tang, J. Han and C. W. Zhou, *Appl. Phys. Lett*., 2003, **82**, 1613.
22. B. Cheng and E. T. Samulski, *J. Mater. Chem. A*, 2001, **11**, 2901.
23. D. H. Zhang, C. Li, S. Han, X. L. Liu, T. Tang, W. Jin and C. W. Zhou, *Appl. Phys. Lett*., 2003, **82**, 112.
24. X.H. Sun, H. R. Hao, H. M. Ji, X. L. Li, S. Cai and C. M. Zheng. *Appl. Mater. Interfaces*, 2014, **6**, 401.
25. A. N. Bondarchuk, J. A. Aguilar-Martinez and M. I. Pech-Canul, *Ceram. Int*., 2014, **40**, 11533.
26. H. Liu, X. He, Y. Hu, X. Liu, H. Jia and B. Xu, *Mater. Lett.* , 2014, **131**, 104.
27. V. G. Myagkov, I. A. Tambasov, O. A. Bayukov, V. S. Zhigalov, L. E. Bykova, Y. L. Mikhlin, M. N. Volochaev and G. N. Bondarenko, *J. Alloy. Compd*., 2014, **612**, 189.
28. S. Niyomkarn, T. Puangpetch and S. Chavadej, *Mat. Sci. Semicon. Proc*., 2014, **25**, 112.
29. K. S. Park, C. G. Lee, H. S. Hong, I. S. Lee and S. J. Kwon. *Ceram. Int*., 2014, **40**, 11727.
30. S. Trocino, P. Frontera, A. Donato, C. Busacca, L. A. Scarpino, P. Antonucci and G. Neri, *Mater. Chem. Phys*., 2014, **147**,.
31. Q. J. Wang, Q. H. Tan and Y. K. Liu, *Physica. B*, 2014, **450**, 54.
32. Y. Wang, B. Liu, D. Cai, H. Li, Y. Liu, D. Wang, L. Wang, Q. Li and T. Wang, *Sensor. Actuat. B-Chem*., 2014, **201**, 351.
33. J. Yin and H. S. Cao, *Inorg. Chem*., 2012, **51**, 6529.
34. L. Y. Chen, Z. X. Wu and Z. D. Zhang, *New J. Chem*., 2009, **33**, 1109.
35. W. Yang, P. Wan, X. Zhou, J. Hu, Y. Guan and L. Feng, *Sensor. Actuat. B-Chem*., 2014, **201**, 228.
36. X. Xu and X. Wang, *Inorg. Chem*., 2009, **48**, 3890.
37. Z. B. Zhuang, Q. Peng, J. F. Liu, X. Wang and Y. D. Li, *Inorg. Chem*., 2007,**46**,5179
38. W. D. Shi, S. Y. Yong and H. J. Zhang, *Chem. Soc. Rev*., 2013, **42**, 5714.
39. W. H. Zhang, F. Wang and W. D. Zhang, *Dalton. T*, 2013, **42**, 4361.
40. W. D. Shi, R. W. Hughes, S. J. Denholme and D. H. Gregory, *CrystEngComm*, 2010, **12**, 641.
41. J. Wang, D. N. Tafen, J. P. Lewis, Z. Hong, A. Manivannan, M. Zhi, M. Li and N. Wu, *J. Am. Chem. Soc.*, 2009, **131**, 12290.

42. T. J. Zhu, X. Chen, Y. Q. Cao and X. B. Zhao, *J. Phys. Chem. C.*, 2009, **113**, 8085.

43. M. Curreli, C. Li, Y. H. Sun, B. Lei, M. A. Gundersen, M. E. Thompson and C. W. Zhou, *J .Am. Chem. Soc.*, 2005, **127**, 6922.

44. Y. h. Yan, Z. H. Zhou, Y. Cheng, L. L. Qiu, C. P. Gao and J. Z. Zhou, *J. Alloy. Compd*, 2014, **60**5,102.

45. S. J. Liang, R. W. Liang, L. R. Wen, R. S. Yuan, L. Wu and X. Z. Fu, *Appl. Catal. B*, 2012, **125**, 103.

46. R. Asahi, T. Morikawa, T. Ohwaki, K. Aoki and Y. Taga, *Science*, 2002, **25**, 626.

47. J. G. McEvoy and Z. S. Zhang, *J. Photoch. Photobio. C*, 2014, **19**, 62

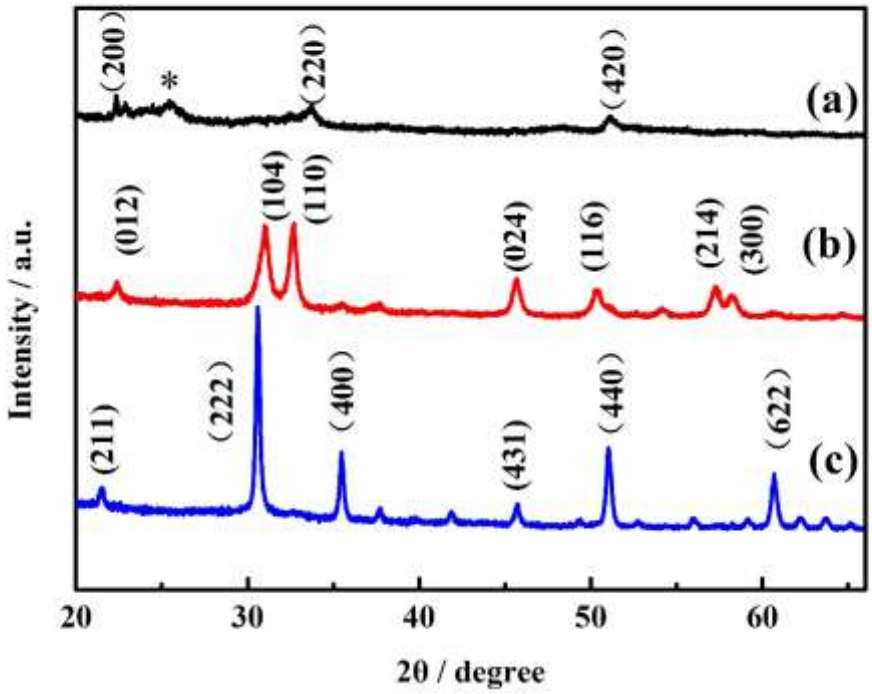

Fig.1. XRD patterns of 3D flower-like the $In(OH)_3$ nanostructures (a); 3D flower-like porous *rh*-In_2O_3 nanostructures (b); and 3D flower-like *c*-In_2O_3 nanostructures (c).

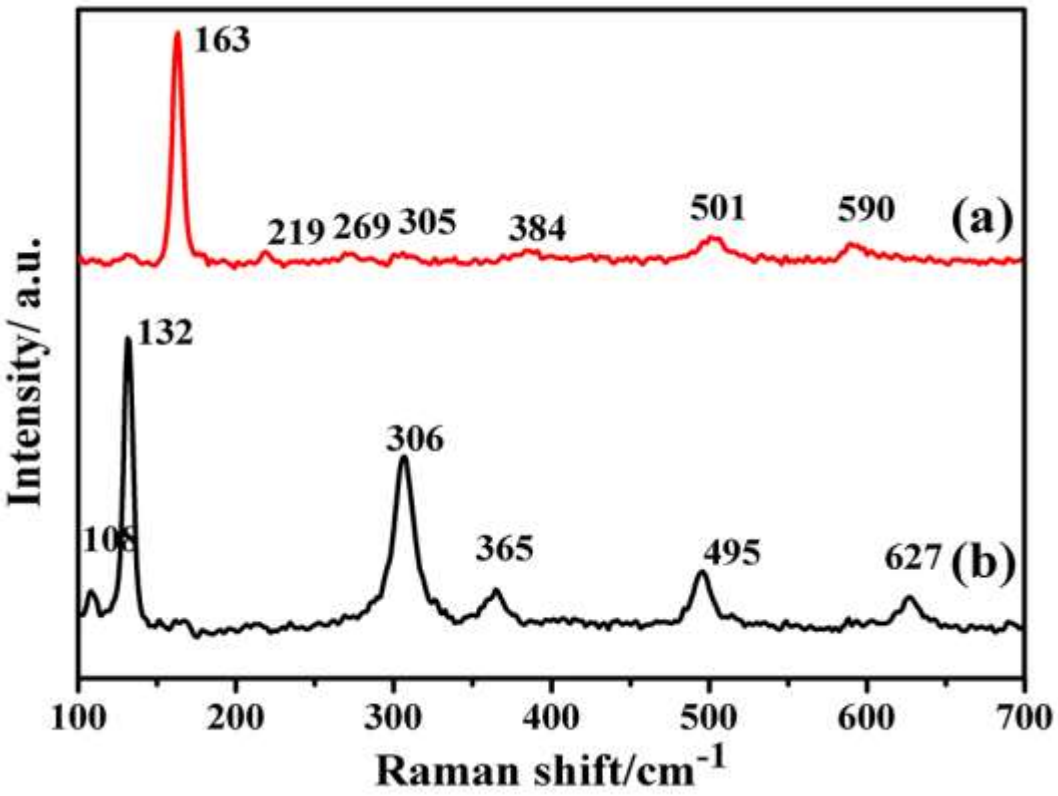

Fig.2. Raman spectra of 3D flower-like porous *rh*-In_2O_3 nanostructures (a), and 3D flower-like *c*-In_2O_3 nanostructures (b).

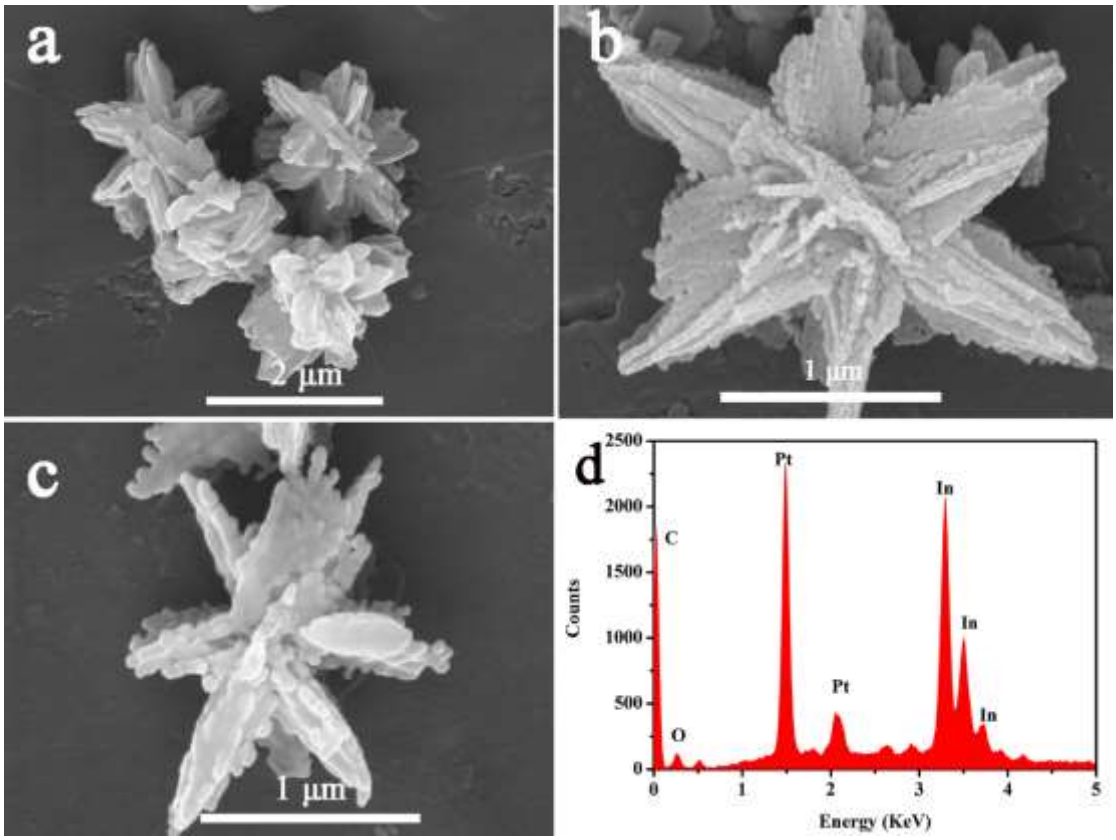

Fig.3. SEM images of the precursor (a); 3D flower-like porous *rh*-In_2O_3 nanostructures (b) and 3D flower-like *c*-In_2O_3 nanostructures (c) obtained by annealing the precursor at 500 ºC and 600 ºC, respectively; (d) EDS of 3D flower-like porous *rh*-In_2O_3 nanostructures.

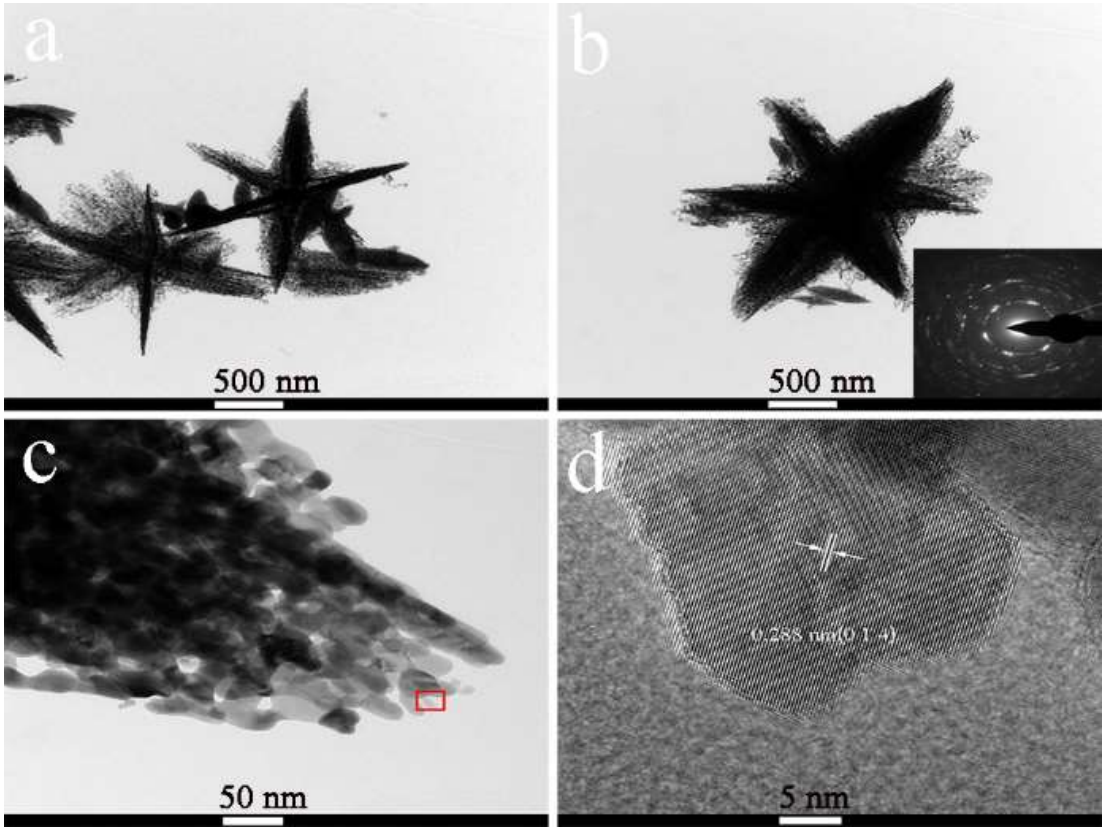

Fig.4. TEM (a-c) and HRTEM (d) images of the 3D flower-like porous *rh*-In_2O_3 nanostructures; and the inset: corresponding SAED pattern.

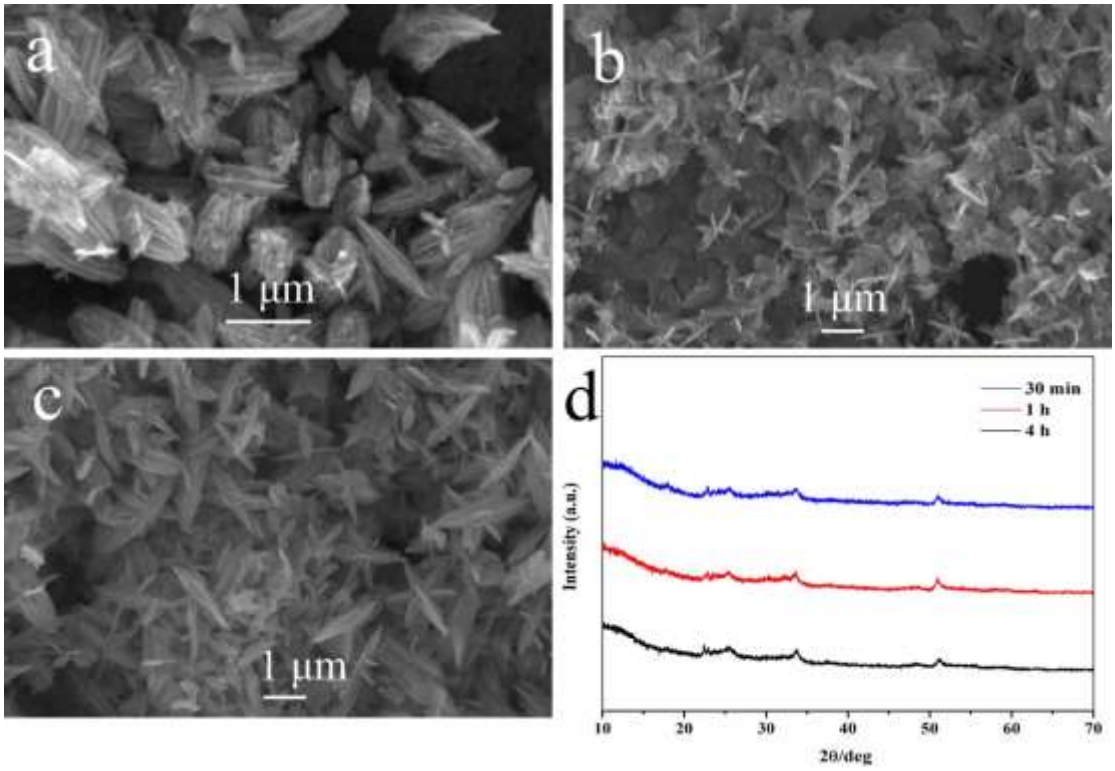

Fig.5. SEM images and XRD patterns of the products collected at different hydrothermal times: (a) 30 min; (b) 1 h; and (c) 4 h.

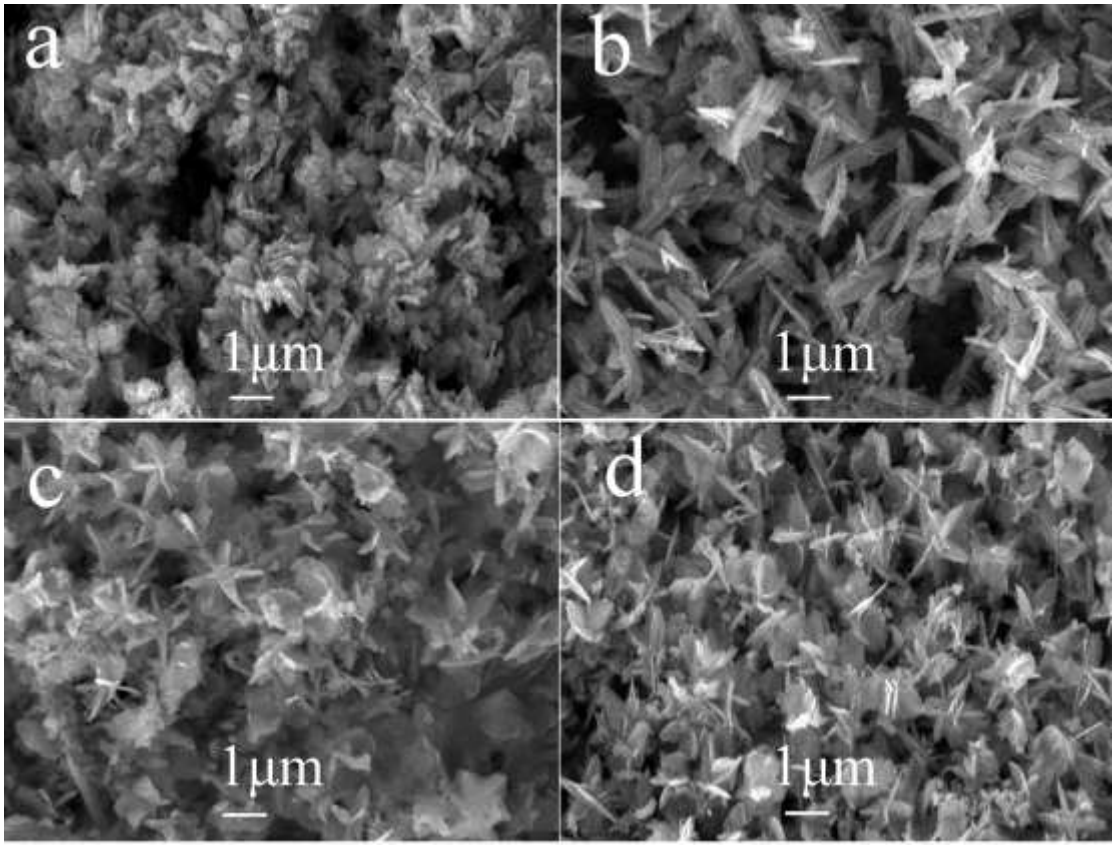

Fig.6. SEM images of the samples obtained with different amounts of glucose (a) 0 mmol; (b) 3 mmol; (c) 7 mmol; and (d) 12 mmol after annealing at 500 ºC (with the same addition of 7 mmol urea).

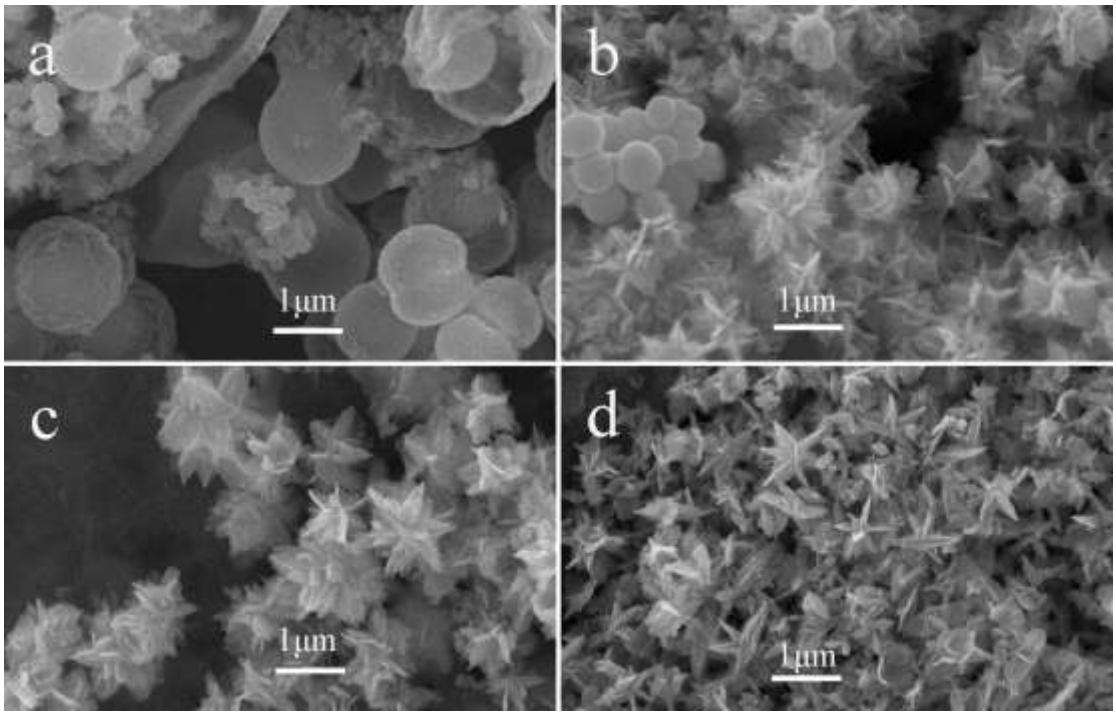

Fig.2. SEM images of the samples obtained with different amounts of urea (a) 0 mmol; (b) 1 mmol; (c) 4 mmol; and (d) 10 mmol after annealing at 500 ºC (with the same addition of 9 mmol glucose).

Scheme 1: the formation of 3D flower-like In_2O_3 nanostructures.

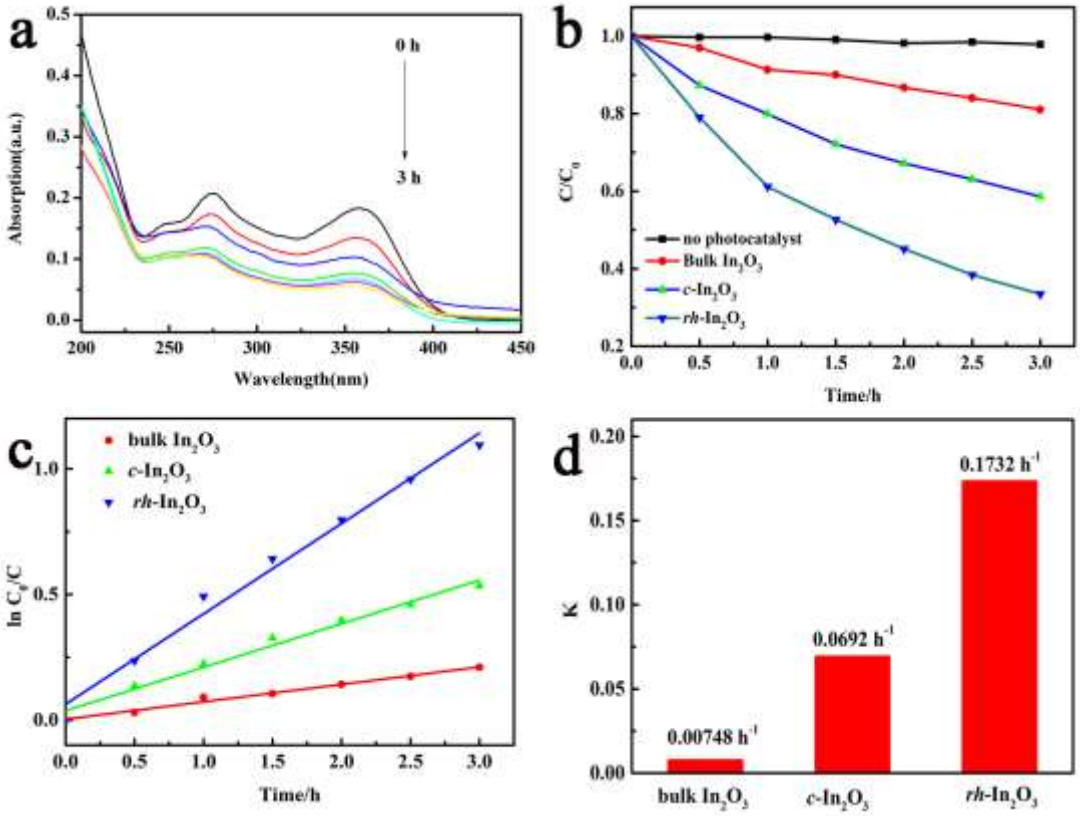

Fig.8. (a) Variation curves of the visible light absorption spectrum of TC in the presence of 3D flower-like rh-In2O3 nanostructures; (b) photodegradation curves of TC in the presence of 3D flower-like porous *rh*-In_2O_3 nanostructures, 3D flower-like *c*-In_2O_3 nanostructures, and bulk In_2O_3; (c) Linear fitting curves of TC degradation; (d) degradation rate constant *k* of samples.

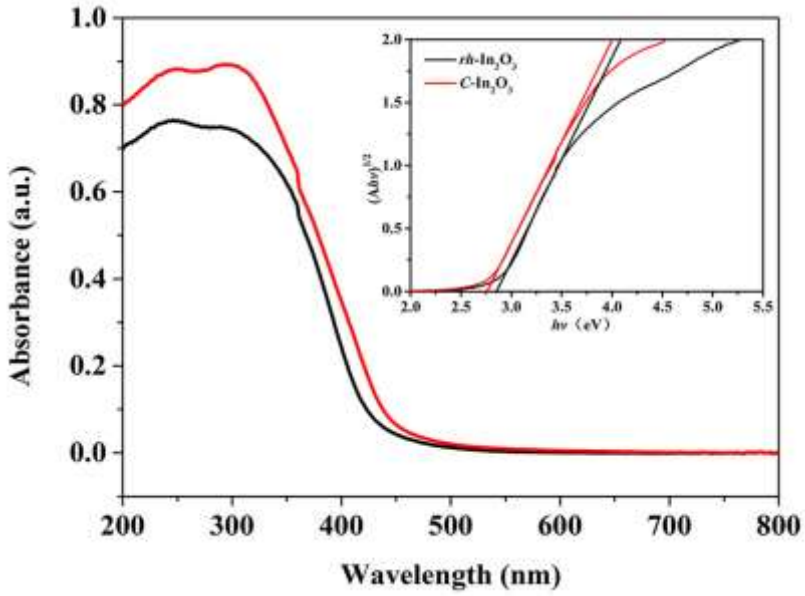

Fig.9. UV-vis absorption spectrum of 3D flower-like porous *rh*-In_2O_3 nanostructures and 3D flower-like *c*-In_2O_3 nanostructures. Inset: the corresponding plot of $(Ahv)^{1/2}$ as a function of photon energy (hv).

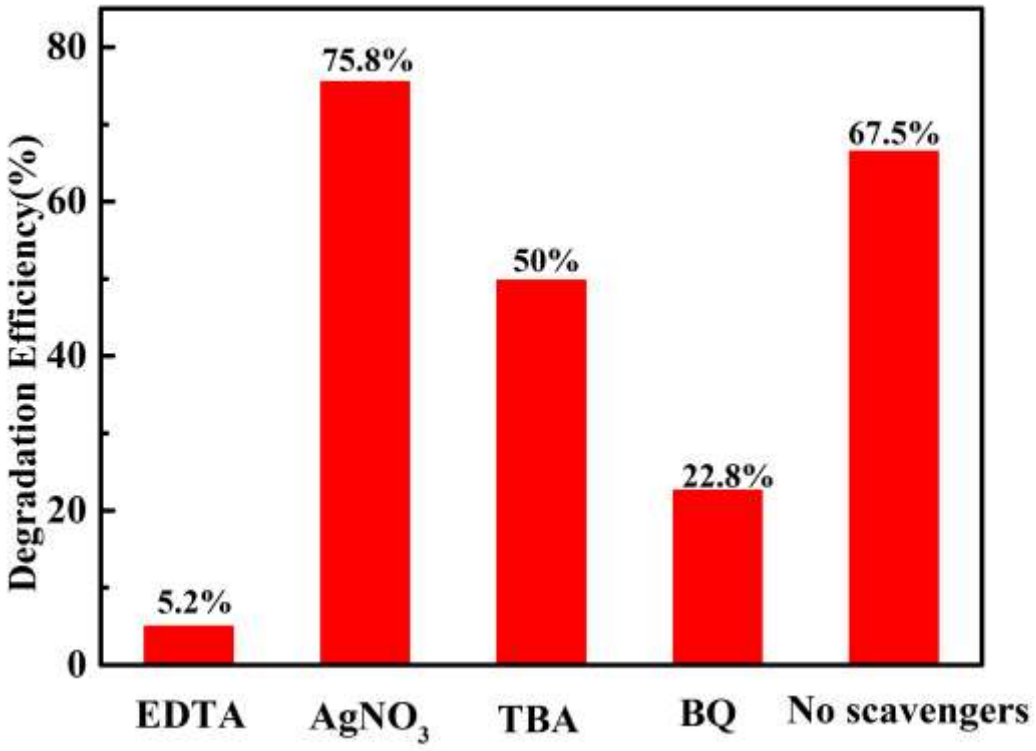

Fig.10. Effects of a series of scavengers on the photodegradation efficiency of TC using 3D flower-like porous *rh*-In_2O_3 nanostructures.

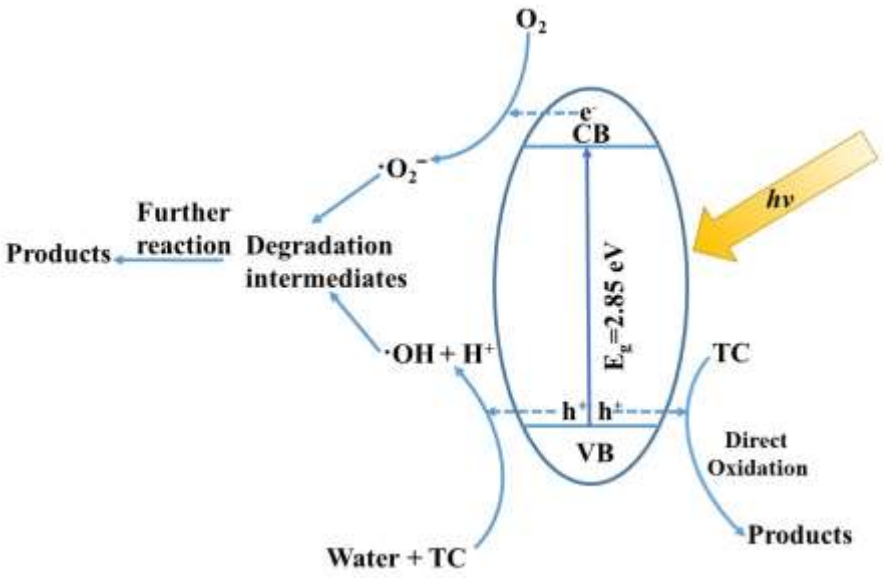

Scheme 2: The degradation mechanism of 3D flower-like porous *rh*-In_2O_3 nanostructures photocatalytic.